CrossMark

PROGRAMMABLE
MATERIALS

RESEARCH ARTICLE

Stabilise and symmetrise the deformation of buckling metamaterial for tunable vibration bandgaps

Encai Liu [1,2], Xin Fang[2], Peidong Zhu[1] and Jihong Wen[2]

[1]Department of Electronic Information and Electrical Engineering, Changsha University, Changsha, China.
[2]Laboratory of Science and Technology on Integrated Logistics Support, College of Intelligent Science and Technology, National University of Defense Technology, Changsha, China.

Corresponding author: Xin Fang; Email: xinfangdr@sina.com

Abstract

Mechanical metamaterials have attracted extensive attention. This paper reports a metamaterial with tunable elastic wave bandgaps based on bistable buckling structure. First, we find that deformation of two symmetric buckling shells is intrinsically asymmetric, which blocks the realisation of robust tunability. Based on an analytical model, we clarify that the mechanisms for this intrinsic asymmetricity are the bifurcations on force–deformation curves. Then we propose a superposition method of buckling shells, which can realise the symmetric deformation for robust tunable stiffness. Using this variable-stiffness oscillator, we design a metamaterial sandwich beam, and numerically and experimentally demonstrate its tunable bandgap for vibration suppression. This paper presents the unusual deformation process of buckling elements widely used for constructing metamaterials, and provides a robust way to realise metamaterials with tunable vibration bandgaps.

Contents

Introduction

Mechanical metamaterials (Fang et al., 2022) are artificial composite materials/structures that exhibit extraordinary mechanical properties beyond natural materials. These exotic properties can be realised through customising the periodic unit cells. The unusual dynamic properties of mechanical metamaterials, such as the locally resonant bandgaps, can efficiently suppress low-frequency elastic waves and structural vibration (Bao et al., 2022; Fang et al., 2022). Such metamaterial is called *acoustic/elastic metamaterial* (Sheng et al., 2021; Gao et al., 2022). Recently, active elastic metamaterials with tunable bandgaps attract great attention (Ning et al., 2020; Montgomery et al., 2021). This relies on the mechanically tunable unit cells, especially the variable-stiffness resonators. Bistable/buckling structures (Fan et al., 2020; Tao et al., 2020) can offer snap-through deformation (Hussein et al., 2019) and negative stiffness (Anna et al., 2017). Therefore, they are widely utilised to design mechanical metamaterials (Hang and Li, 2019; Xia et al., 2020; Fang et al., 2022) for vibration isolation and shock protection. Such metamaterials may present negative stiffness (Tan et al., 2020), negative Poisson's ratio (Rafsanjani and Pasini, 2016; Yang and Ma 2020), reconfigurability (Faber et al., 2020; Khajehtourian and Kochmann, 2021), programmability (Overvelde et al., 2016; Sengupta and Li, 2018), and tunable mechanical properties (Slesarenko, 2020). In particular, wave propagation properties in periodic bistable metamaterials have been investigated (Wu et al., 2018; Jin et al., 2020; Liu et al., 2021). The review above shows that periodic bistable metamaterials can provide unusual properties for controlling wave and deformation.

This paper attempts to conceive an elastic metamaterial with tunable bandgaps based on the buckling element. The design relies on the variable-stiffness local resonators consisting of two symmetric buckling shells, as shown in Figure 1(a). This is a typical buckling structure. However, we find and experimentally demonstrate that the deformation of any symmetric buckling shell is intrinsically asymmetric, which blocks the realisation of robust tunability. Actually, as extensively shown in many literatures concerning the metamaterials consisting of bistable unit cells (Correa et al., 2015; Yang and Ma, 2020), the snap-through deformation of unit cells will not appear simultaneously under a quasi-static compressive stress. Instead, they may happen successively or randomly. This is also attributed to the aforementioned intrinsic asymmetric deformation of a symmetric structure, but this has not been clearly understood. In this paper, we establish a mechanical model and clarify the bifurcation mechanisms for this property. Then, to realise a stable tunability of the local resonators, we propose and demonstrate a superposition method of buckling shells to realise the symmetric deformation and tunable stiffness. Using this tunable element, we design a tunable metamaterial beam and study its tunable bandgap for vibration suppression. Simulations and experiments are carried out to demonstrate our design.

Intrinsic asymmetric deformation of symmetric buckling structure

Design of the symmetric buckling shells

As shown in Figure 1, the typical symmetric element consists of two shells connected by a mass, and the material of the shell is rubber. Every shell is a thin-walled taper cone with thickness t. The taper cone is hollow. Thus, it will buckle under compression. The outer radii of the bistable shell at its large and small ends are R and r, respectively. The height of one shell is h. The two shells of the element are completely the same in geometry and are installed symmetrically. As labelled in Figure 1(b), the parameters of the bistable shell in simulations are listed in Table 1.

Phenomena

We analyse the deformation of this symmetric configuration based on finite element method (FEM) and experiments. In FEM, we fix the bottom edge of the bottom bistable shell and apply a compressive
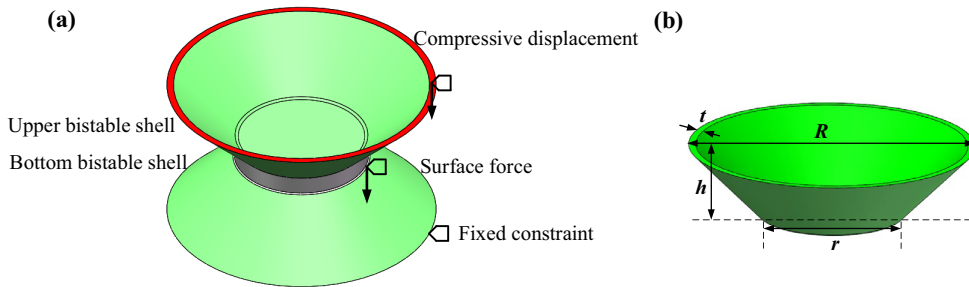
Figure 1. *Variable-stiffness local resonators: (a) Variable-stiffness local resonators consisting of two symmetric buckling shells and its simulation conditions of force disturbance; (b) A buckling shell.*

Table 1. *Parameters of bistable shell in simulations.*

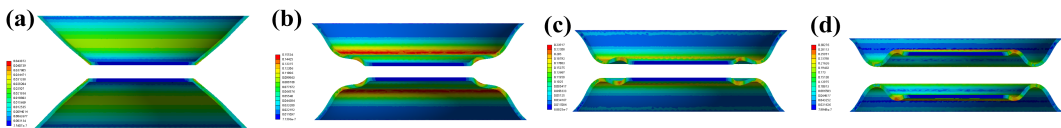| Thickness t	Height h	Large-end radius R	Small-end radius r	Density ρ	Elastic modulus E	Poisson's ratio υ
1 mm	15 mm	30 mm	15 mm	1,300 kg/m³	1.323e7 Pa	0.47

Figure 2. *Deformation of symmetric configuration with completely identical finite element method elements: (a) d = h/15; (b) d = h/3; (c) d = 2h/3; (d) d = 4h/3. The mass block in the centre is not shown here.*

displacement d on the top edge of the upper bistable shell. Moreover, a sweep-meshing technique is adopted to control the element quality in FEM.

First, we make sure that the meshing elements of the upper and bottom shells are symmetric and their structural parameters are identical in the simulation, as shown in Figures 2 and 3. In this ideal case, with the increase of the compression d, the deformation processes of the two bistable shells are completely symmetric, that is, $d_1 = d_2 = d/2$. The force–deformation curve in Figure 3(a) has only one peak, and buckling induces negative stiffness.

However, in practice, due to the imperfections in manufacturing, experimental setups, and material defects, it is impossible to guarantee the ideal symmetrical conditions. Actually, we find that if the meshing elements in the upper and bottom shells are not completely identical, symmetricity will be broken. This means symmetricity will be broken if there is tiny mechanical disturbance, such as the structural parameters, meshing elements in FEM, or force. Here, we show a case with a small gravitational disturbance that generally appears in practice.

As shown in Figure 1(a), we apply a small force 1 N on the upper surface of the bottom bistable shell to simulate the influence of force disturbance on the deformation. When increasing the compressive displacement d, as shown in Figure 4(a,b): First, the bottom bistable shell reaches the critical load and generates snap-through buckling, whereas the upper shell has minimal deformation at this time; then the upper shell reaches the critical load and snaps-through. This means the two geometrically symmetric shells buckle successively instead of simultaneously. Thus, deformation becomes asymmetric. The F–d curve has two peaks and two negative-stiffness stages.

We confirm this property in experiment. The samples are fabricated by rubber. Its geometric parameters are as follows: large radius $R = 28$ mm, small radius $r = 10$ mm, thickness $t = 1$ mm, and height $h = 10$ mm. Although the geometric parameters and material parameters of the bistable shell are
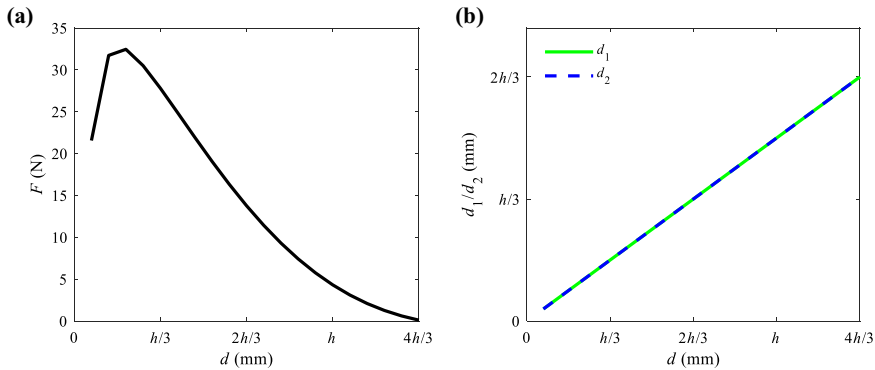
Figure 3. *Simulation results under ideal symmetry condition: (a) Force versus compression curve F–d (F is the force on the symmetric configuration); (b) Deformation of the bistable shell versus compression curve d_1/d_2–d (d_1 and d_2 are the deformations of the upper and bottom shells, respectively).*
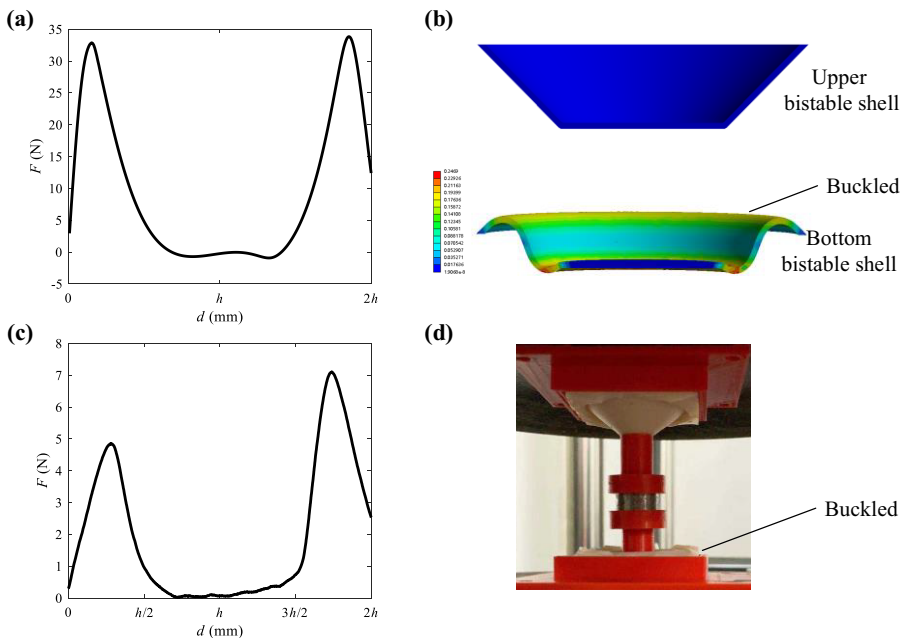

Figure 4. *Finite element method (FEM) results of gravitational disturbance and compression test: (a) F–d curve from the FEM simulation; (b) Deformation from the FEM simulation with compression d = h. The mass block in the centre is not shown. The bottom shell snaps-through first, whereas the upper shell has minimal deformation at this time; (c) F–d curve from the compression test; (d) Deformation with compression d = h from the compression test. The experiments are consistent with the FEM.*

inconsistent with those in the simulation, the intrinsic asymmetric deformation remains. As shown in Figure 4(c,d), the experimental F–d curve in compression shows the identical properties presented in the FEM simulation with gravitational disturbance. The differences of the buckling force in experiments and FEM mainly arise from the material parameters.

The simulation and the experiment demonstrate that the symmetric buckling configuration composed of two symmetrical bistable structures shows asymmetric deformation when compressed in practical mechanical conditions. The two bistable elements snap-through successively.
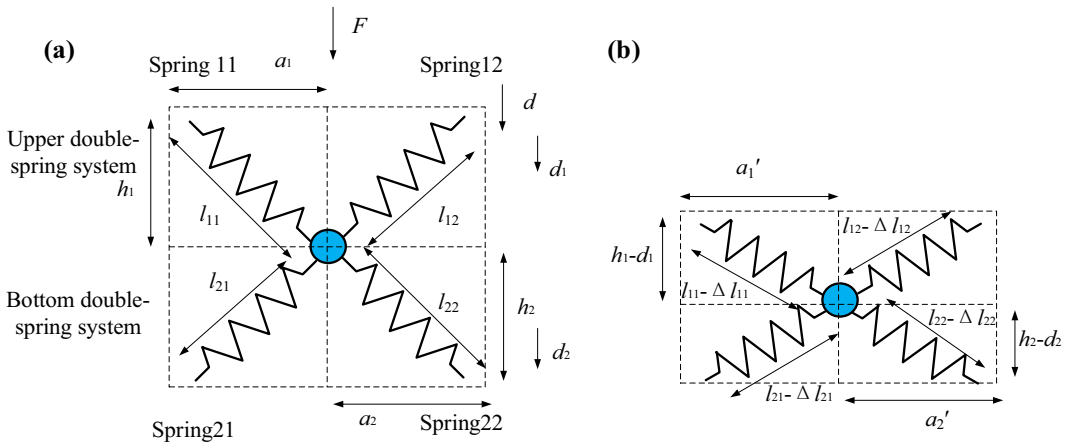
Figure 5. *Symmetric configuration of bistable spring system: (a) Initial configuration; (b) Compressed configuration.*

Mechanism of the asymmetric deformation

We establish a typical model consisting of four springs (i.e., two double-spring systems) to clarify the reason for the asymmetric deformation, as shown in Figure 5. The deformation of the centre point in the horizontal direction is not considered. Springs 11 and 12 form the upper double-spring system (i.e., upper bistable structure), and Springs 21 and 22 form the bottom double-spring system (i.e., bottom bistable structure). The system is compressed by force F, and the vertical compression is d. The vertical displacements of the upper and bottom double-spring systems are denoted by d_1 and d_2, respectively. $d = d_1 + d_2$. The total potential energy of the system is denoted by U. The elastic potential energies of the upper and bottom double-spring systems are denoted by U_1 and U_2, respectively. $U = U_1 + U_2$. Please see Appendix A for all equations and other parameters. The curves and the bifurcations are illustrated in Figure 6.

In Figure 6, all curves with the same labels correspond to the same branch. The deformation of this model features three branches, that is, Branches 1–3. There are two bifurcation points at $d = h$ and $d = 3h$, respectively. Branches 2 and 3 depart from Branch 1 (the black curve marked with '●') at $d = h$ and join with Branch 1 at $d = 3h$. On Branch 1, $d_1 = d_2$, which means that the two double-spring systems deform symmetrically and buckle simultaneously (see Figure 6(b,c)). Here, the system behaves as a single bistable structure. However, Branch 1 has the maximum strain energy at $d = 2h$ (see Figure 6(d–f)), which means that this point is unstable.

Branches 2 and 3 are a pair of solutions satisfying $d = d_1 + d_2$. When a branch appears above Branch 1, the other one appears below Branch 1. Therefore, the two double-spring systems buckle asymmetrically and snap-through in sequence in this case. Moreover, near $d = h$, $\min(d_1, d_2) < 0$, which means that if one double-spring system snaps-through first, the other system is stretched instead of compressed. The potential energy tells the mechanism for the intrinsic asymmetric deformation. As shown in Figure 6(e,f), the potential energy U_1 or U_2 presents as 'N' shape, and the two curves are reversed. As shown in Figure 6(d), the total potential energy curves for Branches 2 and 3 are equal, and they are always smaller than the potential energy on Branch 1. When the potential energy on Branch 1 reaches the maximum at $d = 2h$, the energy on Branch 2 or 3 is zero. At here, one double-spring system snaps-through to the other stable point (without stretch or compression deformation), and the other one recovers to the original stable point without deformation.

The principle of minimum potential energy indicates that the deformation will follow Branch 2 or 3 in practice when $h < d < 3h$. Therefore, the deformation is asymmetric in essence. Considering the bifurcation from Branch 1 to Branches 2 and 3, the F–d curve features two peaks that are consistent with the simulation and the experiment shown in Figure 4.
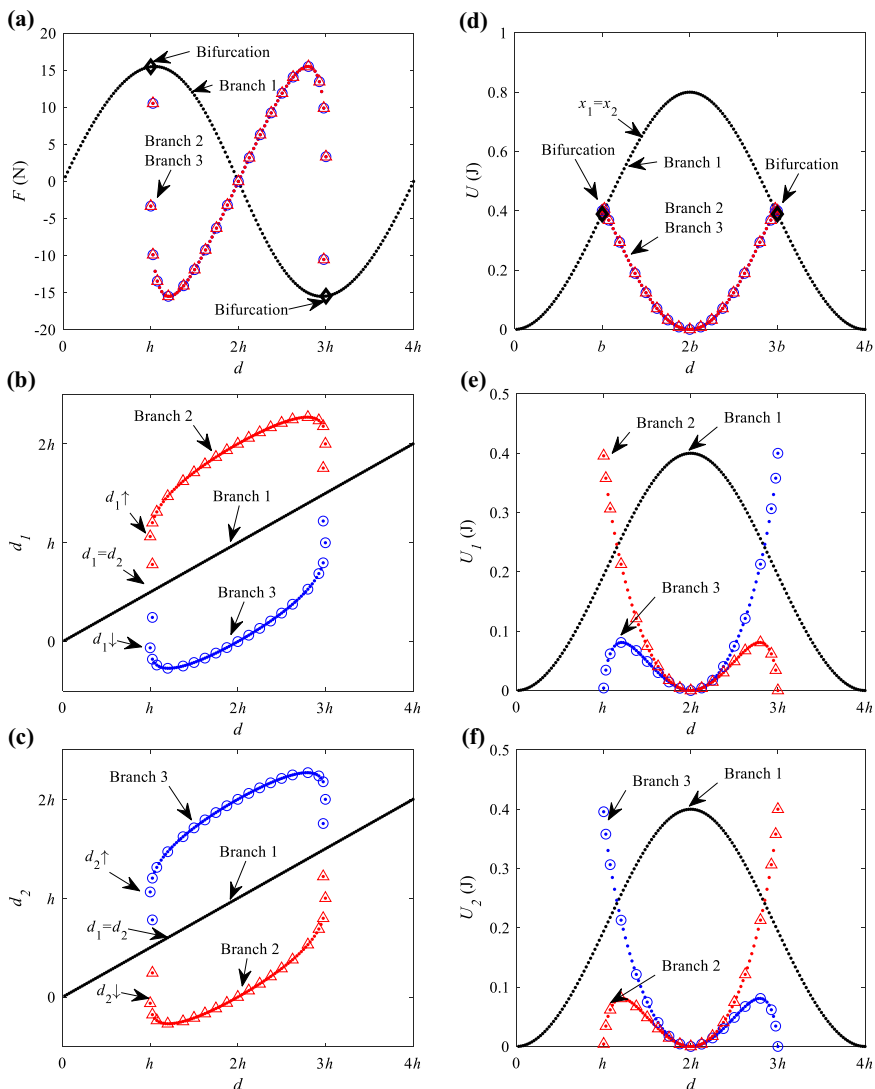
Figure 6. *Symmetric configuration of bistable spring system: (a) F–d curve; (b) Deformation curve of the upper bistable spring system; (c) Deformation curve of the bottom bistable spring system; (d) Total potential energy curve of the symmetric configuration during compression; (e) Potential energy curve of the upper bistable spring system U_1; (f) Potential energy curve of the bottom bistable spring system U_2.*

Variable-stiffness oscillator with symmetric deformation

Model design

To realise a robust variable-stiffness oscillator, we have to make the deformation of the two buckling shells be symmetric, that is, stabilise the deformation. Measures should be taken to make the deformation follows Branch 1 instead of following Branch 2 or 3. Here, we propose a nested design by superimposing several bistable shells, as shown in Figure 7. A bigger shell wraps a smaller one. The lower edges of the four shells are set on the same plane, and the gap between two adjacent shells depends on geometric parameters. Here, the vertical gap between two adjacent shells is 0.5 mm. The upper and bottom teams of shells are symmetric. As shown in Figure 7(b), a cylinder mass block is
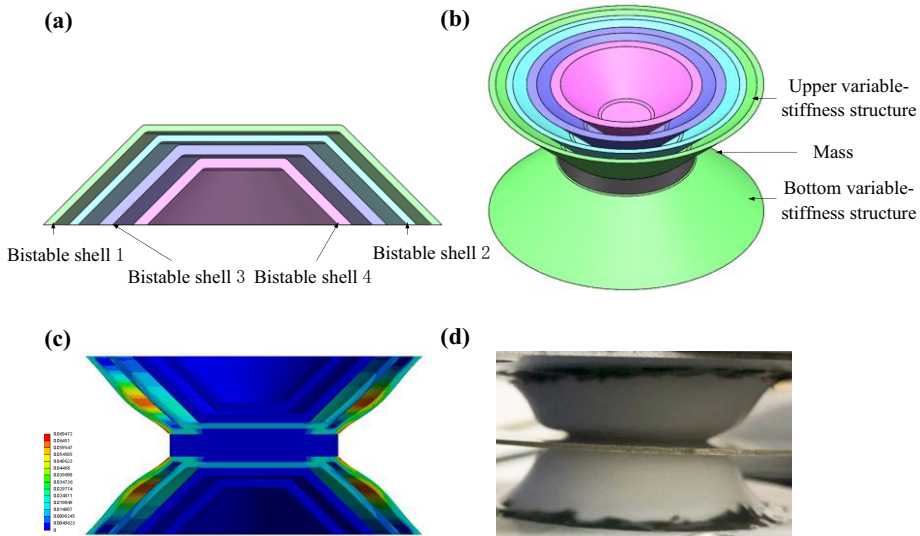
Figure 7. *Variable-stiffness oscillator: (a) Profile of the variable-stiffness structure; (b) Variable-stiffness oscillator model; (c) Strain profile (i.e., the finite element simulation result) of the variable-stiffness oscillator with compression d = 2 mm; (d) Deformation mode (i.e., the compression test result) of the variable-stiffness oscillator with compression d = 2 mm.*

Table 2. *Parameters of bistable shells for constructing variable-stiffness structure.*

Parameters	Shell 1	Shell 2	Shell 3	Shell 4
Thickness t (mm)	1	1	1.5	1.5
Height h (mm)	15	13	12	10
Small radius r (mm)	15	12.5	9.5	6
Large radius R (mm)	30	26.25	21.75	16.55
Density ρ (kg/m^3)	1,300	1,300	1,300	1,190
Elastic modulus E (Pa)	3.6187e6	1.32333e7	4.4e7	2.2e9
Shore hardness HA	60	85	92	Plastic
Poisson's ratio υ	0.47	0.47	0.47	0.375

inserted between them. Parameters of these shells are listed in Table 2. When an outer soft shell is buckled or compressed, it contacts the inner one. Thus, the stiffness is increased, and the inner one will stabilise the deformation to be symmetric. The stiffness of variable-stiffness structure is shown in Appendix B. The deformation of this design is shown in Figure 7(c,d).

The material parameters and structural parameters of the bistable shell (as shown in Table 2) have an effect on the initial stiffness, critical load, critical load location, and other characteristics of the stiffness characteristics. The stiffness of the four shells (mainly the initial stiffness) are superimposed according to the designed configuration, and the total stiffness after superposition is the nonlinear stiffness of the designed variable-stiffness structure, which can be adjusted by changing the parameters of the bistable shells.

Symmetrical deformation

We still use the disturbance of gravitation force to inspect the deformation in simulation. A force 1 N is applied on the mass block. As shown in Figure 7(c,d), the deformations of the two variable-stiffness
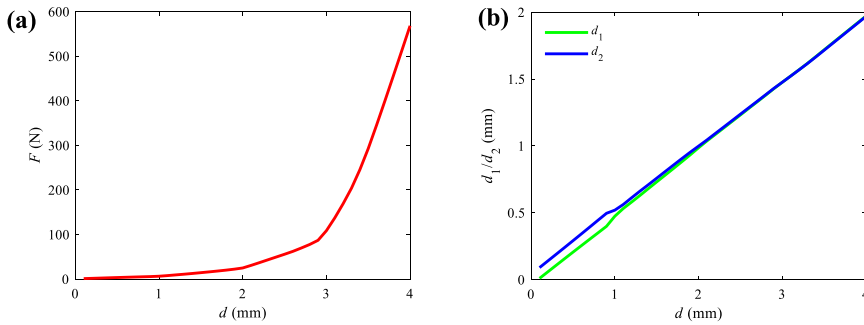
Figure 8. *Force disturbance of oscillator: (a) F–d curve during compression; (b) Deformation of the variable-stiffness structures during compression.*
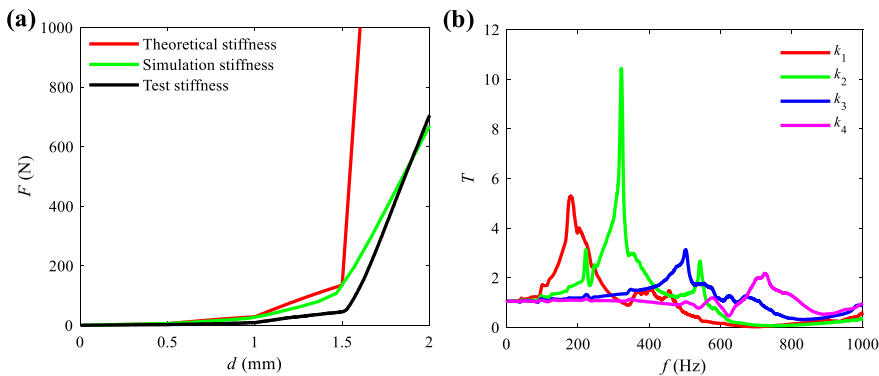

Figure 9. *Tunable property: (a) Tunability of stiffness property; (b) Tunability of dynamic property.*

structures are almost symmetrical under this disturbance. The *F–d* curve shown in Figure 8(a) indicates that the structural stiffness (the slope of the *F–d* curve) increases with the increasing compression *d*. Moreover, we get a large tunable range for the stiffness within a deformation of 4 mm. As shown in Figure 8(b), at the beginning, due to the disturbing force, the deformation of the bottom variable-stiffness structure d_2 is larger than that of the upper structure d_1. With the compression increases, the two deformation curves gradually coincide and $d_1 = d_2 = d/2$: the symmetric deformation is realised.

Therefore, this variable-stiffness oscillator can realise a wide range of stiffness and symmetrical deformation. The asymmetric disturbance makes the initial deformation be slightly different. However, when the compression increases, the deformation of the variable-stiffness oscillator will rapidly self-regulate to be completely symmetric. The reason is that the hardening stiffness of the variable-stiffness oscillator can effectively prevent the asymmetric deformation during compression. We compare the theoretical and experimental deformation curves in Figure 9(a), and they are consistent. Thus, we can adopt the variable-stiffness structure to realise a tunable-frequency resonator that is prepared for the following elastic metamaterial.

Tunable resonant frequency

We conduct vibration tests on the variable-stiffness oscillator to study the variations of resonant frequency. The stiffness is controlled by initial compression of the shells. The centre mass is 45 g and is constant. As shown in Figure 9(b), through increasing the compression, the resonant frequency (the peak value) gradually shifts to high frequency, that is, 179 Hz (k_1) → 323 Hz (k_2) → 503 Hz (k_3) → 723 Hz (k_4). This is a broad tunable range desired for constructing tunable mechanical metamaterials.

Metamaterial beam with tunable vibration bandgaps

Metamaterial design

Based on the variable-stiffness oscillator with symmetrical deformation, we construct a metamaterial structure with tunable bandgaps for efficient vibration reduction. The metamaterial beam is a sandwich structure, as shown in Figure 10(a). The oscillator is periodically inserted between two sheets and act as the local resonators of the elastic metamaterial. Locally resonant bandgap will be generated near the resonant frequency of these oscillators. The bolts and nuts are utilised to control the distance between the two sheets. In this way, we can control the compression to change the stiffness of the resonators. Then the bandgap of the metamaterial sandwich beam will be changed. The width of the metamaterial beam is 110 mm, the thickness is 40 mm, and the lattice constant is 80 mm.

Tunable bandgaps

In order to study the tunable bandgap, the superposed shells are equivalent to a homogeneous variable-stiffness rubber cylinder to calculate dispersion curves, as shown in Figure 11. The mass of every rubber cylinder equals to the mass of a team of shells. One can change the cylinder's elastic modulus to make its stiffness equal to the variable-stiffness structure. The equivalent parameters are shown in Table 3.

Then we adopt the periodic boundary conditions to calculate the dispersion curves of the variable-stiffness metamaterial based on FEM, as shown in Figure 12, where the abscissa is the normalised wavenumber, and the ordinate is the eigenfrequency calculated from the wavenumber. It can be seen
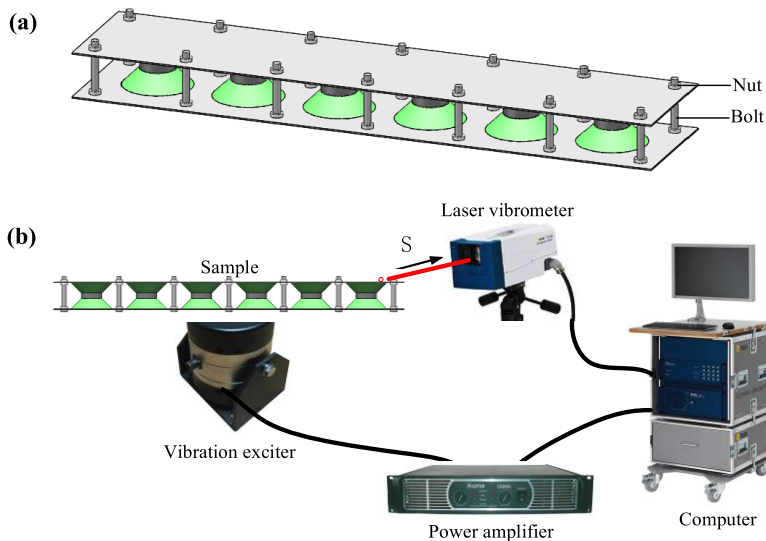
Figure 10. *Tunable metamaterial: (a) Model; (b) Configuration of sandwich beam vibration test.*

Table 3. *Parameters of the homogeneous rubber cylinder equivalent to different stiffness.*

Dynamic stiffness k (N/m)	Length l (mm)	Area A (mm^2)	Elastic modulus E (Pa)	Density ρ (kg/m^3)
5.5781e4	15	706.8583	1.1864e6	1,310.9
1.8167e5	14.5	706.8583	3.7267e6	1,356.2
4.3914e5	14	706.8583	8.6976e6	1,404.6
9.0901e5	13.5	706.8583	1.73608e7	1,456.6
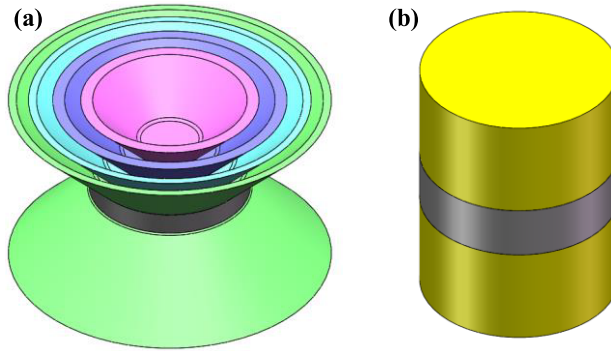
Figure 11. *Equivalent of the variable-stiffness oscillator: (a) Variable-stiffness oscillator; (b) Homogeneous rubber cylinder.*
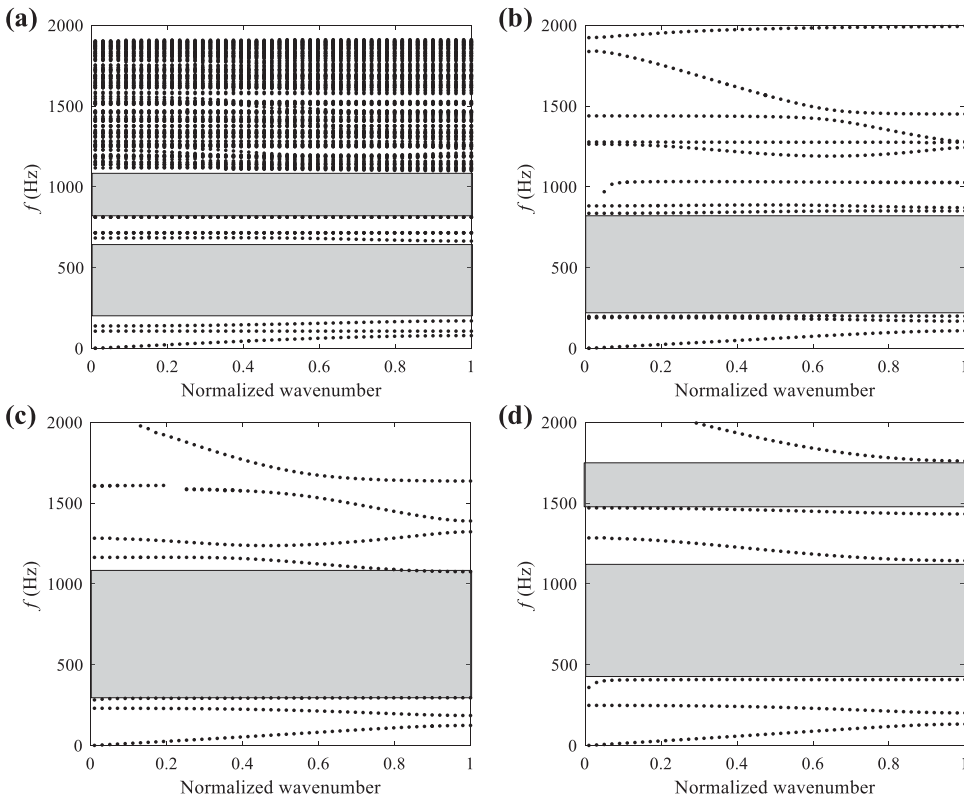
Figure 12. *Dispersion curves of tunable metamaterial: (a) Compression $d_1 = 1$ mm; (b) Compression $d_2 = 2$ mm; (c) Compression $d_3 = 3$ mm; (d) Compression $d_4 = 4$ mm.*

that, in 0–2,000 Hz, the location and width of the bandgaps are tunable by compression, as shown in Table 4. With the increase of compression, the starting frequency of the first bandgap shifts to high frequency, and the bandgap width is widened. In addition, we have investigated the frequency response of the tunable metamaterial and the results are shown in Appendix C.

Experiments

We fabricate a six-period sandwich beam using the geometric parameters and material parameters listed in Table 2. The constant mass of the resonator is 45 g. Figure 10(b) shows the configuration of the

Table 4. *Bandgaps of the tunable metamaterial with different compressions.*

Compression (mm)	Dynamic stiffness (N/m)	Bandgap location (Hz)	Bandgap width (Hz)
$d_1 = 1$	5.5781e4	170–664	494
		813–1,105	292
$d_2 = 2$	1.8167e5	200–835	635
$d_3 = 3$	4.3914e5	295–1,076	781
$d_4 = 4$	9.0901e5	408–1,140	724
		1,434–1,761	241
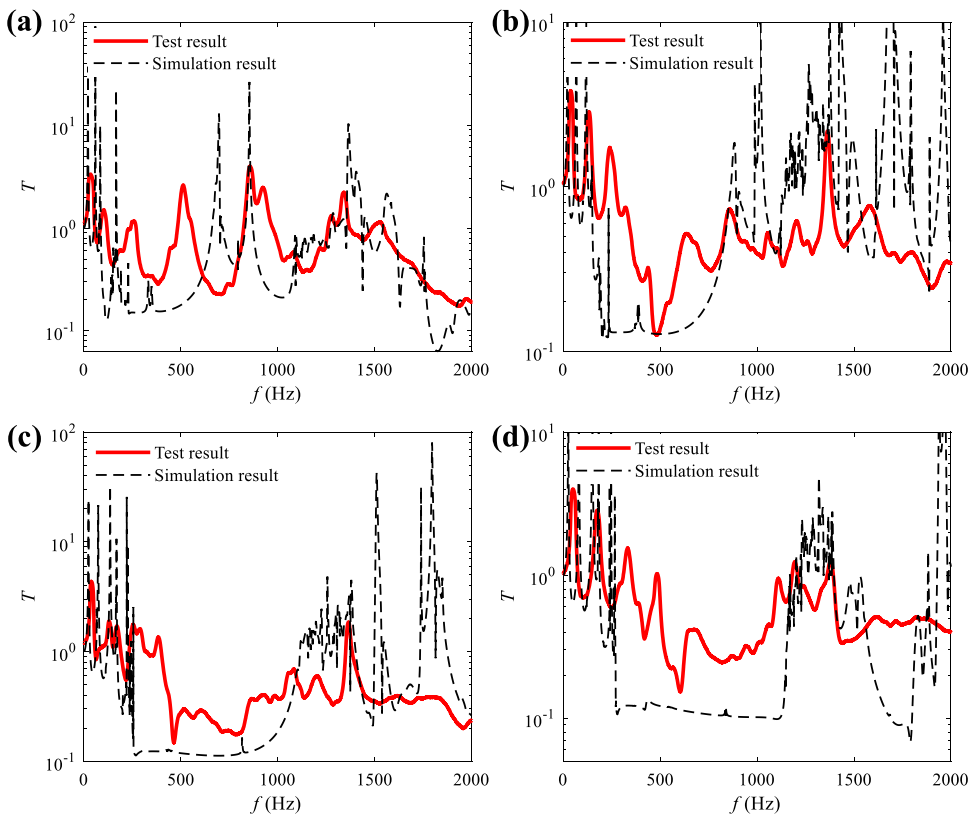
Figure 13. *Comparison between the test results and simulation results of the sandwich beam: (a) Compression $d_1 = 1$ mm; (b) Compression $d_2 = 2$ mm; (c) Compression $d_3 = 3$ mm; (d) Compression $d_4 = 4$ mm.*

sandwich beam in the vibration test. The transverse excitation signal is applied at the middle point of a face sheet. We use a laser vibrometer to measure the average response on the other face sheet of the sample, V_{av}. The excitation velocity is V_0. The vibration transmission $T = V_{av}/V_0$. The stiffness of the system is adjusted by compressing variable-stiffness oscillators. Moreover, we perform FEM simulation for the 0–2,000 Hz frequency responses of this metamaterial sandwich beam. The boundary conditions in the simulation are identical with the experiment.

The comparison of vibration transmissibility between the test results and the simulation results under different compressions is shown in Figure 13. The vibration test results and the finite element simulation

results show that the location and width of the attenuation zone are consistent with the bandgap range shown in Figure 12. With the increase of stiffness, the starting frequency of the vibration attenuation zone shifts to high frequency, and the zone with high attenuation efficiency (transmissivity $T \approx 10^{-1}$) widens to high frequency. Therefore, the tunable bandgap enables the tunable and broadband vibration suppression.

Conclusions

In this paper, we stabilise and symmetrise the deformation of buckling structure to design an elastic metamaterial with tunable bandgaps. The main results are summarised as follows:

1. Based on finite element simulation and experimental test, we find that a symmetric element composed of two bistable structures can present symmetric deformation only under strictly symmetric mechanical conditions. In practice, due to uncertainties, symmetricity of the deformation is broken, and the two bistable structures snap-through successively instead of simultaneously. A general model is established to clarify the mechanism for this intrinsic asymmetric deformation: bifurcations of force–deformation curves. The curve has three branches. Symmetricity is broken because the deformation actually follows the pair of branches with minimum potential energy.
2. A variable-stiffness oscillator with symmetrical deformation is designed by superposing multiple bistable shells, and the robustness and stable tuning ability of the variable-stiffness oscillator is validated with finite element simulation and test.
3. Based on the local resonance mechanism, we design a tunable metamaterial sandwich beam using the variable-stiffness oscillators. Tunable bandgaps and vibration responses are extensively studied by simulation and vibration test.

In conclusion, this paper investigates the mechanical property of the tunable metamaterial and its wave attenuation characteristics using bandgaps. The results are significant for the design of metamaterials using buckling elements, and the paper provides a way to realise metamaterials with tunable vibration bandgaps.

References

Anna GI, **Ricardo FA**, **Geoffrey M** and **Lorenzo V** (2017) Optimal design of a cellular material encompassing negative stiffness elements for unique combinations of stiffness and elastic hysteresis. *Materials and Design* **135**, 37–50.

Bao HH, **Wu CY**, **Zheng WG** and **Yan B** (2022) Low-frequency bandgaps of the lightweight single-phase acoustic metamaterials with locally resonant Archimedean spirals. *Materials* **15**, 1–13.

Correa DM, **Klatt T**, **Cortes S**, **Haberman M**, **Kovar D** and **Seepersad C** (2015) Negative stiffness honeycombs for recoverable shock isolation. *Rapid Prototyping Journal* **21**, 193–200.

Faber JA, **Udani JP**, **Riley KS**, **Studart AR** and **Arrieta AF** (2020) Dome-patterned metamaterial sheets. *Advanced Science* **7**, 2001955.

Fan HG, **Tian YC**, **Yang LJ**, **Hu DP** and **Liu PQ** (2020) Multistable mechanical metamaterials with highly tunable strength and energy absorption performance. *Mechanics of Composite Materials and Structures* **1**, 1–13.

Fang X, **Sheng P**, **Wen JH**, **Chen WQ** and **Cheng L** (2022) A nonlinear metamaterial plate for suppressing vibration and sound radiation. *International Journal of Mechanical Sciences* **228**, 107473.

Fang X, **Wen JH**, **Cheng L**, **Yu DL**, **Zhang HJ** and **Gumbsch P** (2022) Programmable gear-based mechanical metamaterials. *Nature Materials* **21**, 869–876.

Fang ST, **Zhou SX**, **Yurchenko D**, **Yang T** and **Liao WH** (2022) Multistability phenomenon in signal processing, energy harvesting, composite structures, and metamaterials: A review. *Mechanical Systems and Signal Processing* **166**, 108419.

Gao YQ, **Wang LF**, **Sun W**, **Wu K** and **Hu HY** (2022) Ultrawide bandgap in metamaterials via coupling of locally resonant and Bragg bandgaps. *Acta Mechanica* **33**, 477–493.

Hang Y and **Li M** (2019) Multi-stable mechanical metamaterials by elastic buckling instability. *Journal of Materials Science* **54**, 3509–3526.

Hussein H, **Moal PL**, **Younes R**, **Bourbon G**, **Haddab Y** and **Lutz P** (2019) On the design of a preshaped curved beam bistable mechanism. *Mechanism and Machine Theory* **131**, 204–217.

Jin LS, **Khajehtourian R**, **Mueller J**, **Rafsanjani A**, **Tournat V**, **Bertoldi K** and **Kochmann DM** (2020) Guided transition waves in multistable mechanical metamaterials. *Proceedings of the National Academy of Sciences of the United States of America* **117**, 2319–2325.

Khajehtourian R and **Kochmann DM** (2021) A continuum description of substrate-free dissipative reconfigurable metamaterials. *Journal of the Mechanics and Physics of Solids* **147**, 104217.

Liu EC, **Fang X** and **Wen JH** (2021) Harmonic and shock wave propagation in bistable periodic structure: Regularity, randomness, and tunability. *Journal of Vibration and Control* **28**, 3332–3343.

Montgomery SM, **Wu S**, **Kuang X**, **Armstrong CD**, **Zemelka C**, **Ze QJ**, **Zhang RD**, **Zhao RK** and **Qi HJ** (2021) Magneto-mechanical metamaterials with widely tunable mechanical properties and acoustic bandgaps. *Advanced Functional Materials* **31**, 2005319.

Ning L, **Wang YZ** and **Wang YS** (2020) Active control cloak of the elastic wave metamaterial. *International Journal of Solids and Structures* **202**, 126–135.

Overvelde JTB, **Jong TA** and **Shevchenko Y** (2016) A three-dimensional actuated origami-inspired transformable metamaterial with multiple degrees of freedom. *Nature Communications* **7**, 10929.

Rafsanjani A and **Pasini D** (2016) Bistable auxetic mechanical metamaterials inspired by ancient geometric motifs. *Extreme Mechanics Letters* **9**, 291–296.

Sengupta S and **Li S** (2018) Harnessing the anisotropic multistability of stacked-origami mechanical metamaterials for effective modulus programming. *Journal of Intelligent Material Systems and Structures* **29**, 2933–2945.

Sheng P, **Fang X**, **Wen JH** and **Yu DL** (2021) Vibration properties and optimized design of a nonlinear acoustic metamaterial beam. *Journal of Sound and Vibration* **492**, 115739.

Slesarenko V (2020) Planar mechanical metamaterials with embedded permanent magnets. *Materials* **13**, 1313.

Tan XJ, **Wang B**, **Zhu SW**, **Chen S**, **Yao K**, **Xu PF**, **Wu LZ** and **Sun YG** (2020) Novel multidirectional negative stiffness mechanical metamaterials. *Smart Materials and Structures* **29**, 015037.

Tao R, **Xi L**, **Wu WW**, **Li Y**, **Liao BB**, **Liu LW**, **Leng JS** and **Fang DN** (2020) 4D printed multi-stable metamaterials with mechanically tunable performance. *Composite Structures* **252**, 112663.

Wu Y, **Chaunsali R**, **Yasuda H**, **Yu K** and **Yang J** (2018) Dial-in topological metamaterials based on bistable Stewart platform. *Scientific Reports* **8**, 112.

Xia YW, **Ruzzene M** and **Erturk A** (2020) Bistable attachments for wideband nonlinear vibration attenuation in a metamaterial beam. *Nonlinear Dynamics* **102**, 1285–1296.

Yang H and **Ma L** (2020) 1D to 3D multi-stable architected materials with zero Poisson's ratio and controllable thermal expansion. *Materials and Design* **188**, 108430.

Yang H and **Ma L** (2020) Angle-dependent transitions between structural bistability and multistability. *Advanced Engineering Materials* **22**, 1–10.

Appendix A: Analysis process of asymmetric deformation mechanism

Figure 5(a) shows the series double-spring system. The system parameters are as follows: (i) the stiffness of the spring 11 is k_{11}, its original length is l_{11}, the horizontal distance from one end to the other end of the spring is a_1, the vertical distance (i.e., the height of the double-spring system) is h_1, and $l_{11} = \sqrt{a_1^2 + h_1^2}$; (ii) the stiffness of the spring 12 is k_{12}, its original length is l_{12}, the horizontal distance from one end to the other end of the spring is a_2, the vertical distance is h_1, and $l_{12} = \sqrt{a_2^2 + h_1^2}$; (iii) the stiffness of Spring 21 is k_{21}, its original length is l_{21}, the horizontal distance from one end to the other end of the spring is a_1, the vertical distance is h_2, and $l_{21} = \sqrt{a_1^2 + h_2^2}$; (iv) the stiffness of Spring 22 is k_{22}, its original length is l_{22}, the horizontal distance from one end to the other end of the spring is a_2, the vertical distance is h_2, and $l_{22} = \sqrt{a_2^2 + h_2^2}$.

Compressed by the vertical force F (Figure 5), the deformations of the four springs are Δl_{11}, Δl_{12}, Δl_{21}, and Δl_{22}, respectively, and the lengths of the four springs become $l_{11} - \Delta l_{11}$, $l_{12} - \Delta l_{12}$, $l_{21} - \Delta l_{21}$, and $l_{22} - \Delta l_{22}$, respectively. The vertical lengths of springs are $h_1 - d_1$ and $h_2 - d_2$, respectively. The horizontal lengths of the springs are $a\prime_1$ and $a\prime_2$.

The system is analysed according to the force balance condition, and the vertical direction of the series system is asymmetric.

The deformations of the springs after compression are

$$
\begin{aligned}
\Delta l_{11} &= l_{11} - \sqrt{(h_1 - d_1)^2 + a_1'^2}, \\
\Delta l_{12} &= l_{12} - \sqrt{(h_1 - d_1)^2 + a_2'^2}, \\
\Delta l_{21} &= l_{21} - \sqrt{(h_2 - d_2)^2 + a_1'^2}, \\
\Delta l_{22} &= l_{22} - \sqrt{(h_2 - d_2)^2 + a_2'^2}.
\end{aligned}
\tag{1}
$$

The spring forces are

$$
\begin{aligned}
F_{11} &= k_{11}\Delta l_{11} = k_{11}\left(l_{11} - \sqrt{(h_1 - d_1)^2 + a_1'^2}\right), \\
F_{12} &= k_{12}\Delta l_{12} = k_{12}\left(l_{12} - \sqrt{(h_1 - d_1)^2 + a_2'^2}\right), \\
F_{21} &= k_{21}\Delta l_{21} = k_{21}\left(l_{21} - \sqrt{(h_2 - d_2)^2 + a_1'^2}\right), \\
F_{22} &= k_{22}\Delta l_{22} = k_{22}\left(l_{22} - \sqrt{(h_2 - d_2)^2 + a_2'^2}\right).
\end{aligned}
\tag{2}
$$

From equations (1) and (2), it can be deduced that, after being compressed, the horizontal force of the two springs on the left side of the vertical asymmetric system to the connection point is

$$
\begin{aligned}
F_{\text{lh}} &= k_{11}\Delta l_{11}\frac{a_1'}{\sqrt{(h_1-d_1)^2+a_1'^2}} + k_{12}\Delta l_{21}\frac{a_1'}{\sqrt{(h_2-d_2)^2+a_1'^2}} \\
&= k_{11}a_1'\left(\frac{l_{21}}{\sqrt{(h_1-d_1)^2+a_1'^2}} - 1\right) + k_{12}a_1'\left(\frac{l_{21}}{\sqrt{(h_2-d_2)^2+a_1'^2}} - 1\right).
\end{aligned}
\tag{3}
$$

The horizontal force of the two springs on the right side of the vertical asymmetric system to the connection point is

$$
\begin{aligned}
F_{\text{rh}} &= k_{21}\Delta l_{12}\frac{a_2'}{\sqrt{(h_1-d_1)^2+a_2'^2}} + k_{22}\Delta l_{22}\frac{a_2'}{\sqrt{(h_2-d_2)^2+a_2'^2}} \\
&= k_{21}a_2'\left(\frac{l_{12}}{\sqrt{(h_1-d_1)^2+a_2'^2}} - 1\right) + k_{22}a_2'\left(\frac{l_{22}}{\sqrt{(h_2-d_2)^2+a_2'^2}} - 1\right).
\end{aligned}
\tag{4}
$$

Combining equations (3) and (4), from the force balance in the horizontal direction of the system, we can obtain

$$
\begin{aligned}
&k_{11}a_1'\left(\frac{l_{11}}{\sqrt{(h_1-d_1)^2+a_1'^2}} - 1\right) + k_{12}a_1'\left(\frac{l_{12}}{\sqrt{(h_2-d_2)^2+a_1'^2}} - 1\right) \\
&= k_{21}a_2'\left(\frac{l_{21}}{\sqrt{(h_1-d_1)^2+a_2'^2}} - 1\right) + k_{22}a_2'\left(\frac{l_{22}}{\sqrt{(h_2-d_2)^2+a_2'^2}} - 1\right).
\end{aligned}
\tag{5}
$$

After being compressed, the vertical force of the upper double-spring in the vertical asymmetric system to the connection point is

$$
\begin{aligned}
F_{1v} &= k_{11}\Delta l_{11}\frac{h_1-d_1}{\sqrt{(h_1-d_1)^2+a_1'^2}} + k_{12}\Delta l_{21}\frac{h_1-d_1}{\sqrt{(h_2-d_2)^2+a_1'^2}} \\
&= k_{11}(h_1-d_1)\left(\frac{l_{21}}{\sqrt{(h_1-d_1)^2+a_1'^2}} - 1\right) + k_{12}(h_1-d_1)\left(\frac{l_{21}}{\sqrt{(h_2-d_2)^2+a_1'^2}} - 1\right).
\end{aligned}
\tag{6}
$$

The vertical force of the bottom double-spring to the connection point is

$$F_{2v} = k_{21}\Delta l_{12}\frac{h_2-d_2}{\sqrt{(h_1-d_1)^2+a_2'^2}} + k_{22}\Delta l_{22}\frac{h_2-d_2}{\sqrt{(h_2-d_2)^2+a_2'^2}}$$

$$= k_{21}\left(h_2-d_2\right)\left(\frac{l_{12}}{\sqrt{(h_1-d_1)^2+a_2'^2}}-1\right) + k_{22}\left(h_2-d_2\right)\left(\frac{l_{22}}{\sqrt{(h_2-d_2)^2+a_2'^2}}-1\right). \tag{7}$$

Combining equations (6) and (7), from the force balance in the vertical direction of the system, we can obtain

$$k_{11}\left(h_1-d_1\right)\left(\frac{l_{21}}{\sqrt{(h_1-d_1)^2+a_1'^2}}-1\right) + k_{12}\left(h_1-d_1\right)\left(\frac{l_{21}}{\sqrt{(h_2-d_2)^2+a_1'^2}}-1\right)$$

$$= k_{21}\left(h_2-d_2\right)\left(\frac{l_{12}}{\sqrt{(h_1-d_1)^2+a_2'^2}}-1\right) + k_{22}\left(h_2-d_2\right)\left(\frac{l_{22}}{\sqrt{(h_2-d_2)^2+a_2'^2}}-1\right), \tag{8}$$

$$F = F_{1v} = k_{11}\left(h_1-d_1\right)\left(\frac{l_{21}}{\sqrt{(h_1-d_1)^2+a_1'^2}}-1\right) + k_{12}\left(h_1-d_1\right)\left(\frac{l_{21}}{\sqrt{(h_2-d_2)^2+a_1'^2}}-1\right). \tag{9}$$

From the deformation relationship in the vertical direction of the system, we can get

$$d_1 + d_2 = d. \tag{10}$$

From the deformation relationship in the horizontal direction of the system, we can get

$$a_1' + a_2' = a_1 + a_2. \tag{11}$$

Combining equations (5) and (8)–(11), a set of equations for the relationship between variables F, d_1, d_2, $a\prime_1$, and $a\prime_2$ and the compression d can be obtained as

$$\begin{cases} k_{11}a_1'\left(\dfrac{l_{11}}{\sqrt{(h_1-d_1)^2+a_1'^2}}-1\right) + k_{12}a_1'\left(\dfrac{l_{12}}{\sqrt{(h_2-d_2)^2+a_1'^2}}-1\right) \\[2mm] = k_{21}a_2'\left(\dfrac{l_{21}}{\sqrt{(h_1-d_1)^2+a_2'^2}}-1\right) + k_{22}a_2'\left(\dfrac{l_{22}}{\sqrt{(h_2-d_2)^2+a_2'^2}}-1\right), \\[2mm] k_{11}\left(h_1-d_1\right)\left(\dfrac{l_{21}}{\sqrt{(h_1-d_1)^2+a_1'^2}}-1\right) + k_{12}\left(h_1-d_1\right)\left(\dfrac{l_{21}}{\sqrt{(h_2-d_2)^2+a_1'^2}}-1\right) \\[2mm] = k_{21}\left(h_2-d_2\right)\left(\dfrac{l_{12}}{\sqrt{(h_1-d_1)^2+a_2'^2}}-1\right) + k_{22}\left(h_2-d_2\right)\left(\dfrac{l_{22}}{\sqrt{(h_2-d_2)^2+a_2'^2}}-1\right), \\[2mm] F = k_{11}\left(h_1-d_1\right)\left(\dfrac{l_{21}}{\sqrt{(h_1-d_1)^2+a_1'^2}}-1\right) + k_{12}\left(h_1-d_1\right)\left(\dfrac{l_{21}}{\sqrt{(h_2-d_2)^2+a_1'^2}}-1\right), \\[2mm] d_1+d_2=d, \\[1mm] a_1'+a_2'=a_1+a_2. \end{cases} \tag{12}$$

In order to simplify the analysis, we ignore the asymmetry in the horizontal direction of double-spring structures, and assume that the deformation in the horizontal direction before and after compression is completely symmetrical.

To satisfy the assumptions, the system needs to satisfy

$$a_1' = a_2' = a_1 = a_2 = a, \tag{13}$$

$$l_{11} = l_{12} = l_1,$$
$$l_{21} = l_{22} = l_2, \tag{14}$$

$$k_{11} = k_{12} = k_1,$$
$$k_{21} = k_{22} = k_2. \tag{15}$$

Correspondingly, the spring deformations are

$$\Delta l_1 = l_1 - \sqrt{(h_1 - d_1)^2 + a^2},$$
$$\Delta l_2 = l_2 - \sqrt{(h_2 - d_2)^2 + a^2}. \tag{16}$$

The spring forces are

$$F_1 = k_1 \Delta l_1 = k_1 \left(l_1 - \sqrt{(h_1 - d_1)^2 + a^2} \right),$$
$$F_2 = k_2 \Delta l_2 = k_2 \left(l_2 - \sqrt{(h_2 - d_2)^2 + a^2} \right). \tag{17}$$

From the force balance in the vertical direction of the system,

$$F = 2k_1 (h_1 - d_1) \left(\frac{l_1}{\sqrt{(h_1-d_1)^2+a^2}} - 1 \right),$$
$$k_1 (h_1 - d_1) \left(\frac{l_1}{\sqrt{(h_1-d_1)^2+a^2}} - 1 \right) = k_2 (h_2 - d_2) \left(\frac{l_2}{\sqrt{(h_2-d_2)^2+a^2}} - 1 \right). \tag{18}$$

Combining equations (12) and (18), a set of equations for the relationship between variables F, d_1, and d_2 and the compression d can be obtained as

$$\begin{cases} F = 2k_1 (h_1 - d_1) \left(\frac{l_1}{\sqrt{(h_1-d_1)^2+a^2}} - 1 \right), \\ k_1 (h_1 - d_1) \left(\frac{l_1}{\sqrt{(h_1-d_1)^2+a^2}} - 1 \right) = k_2 (h_2 - d_2) \left(\frac{l_2}{\sqrt{(h_2-d_2)^2+a^2}} - 1 \right), \\ d_1 + d_2 = d. \end{cases} \tag{19}$$

In the initial state, when the two double-spring structures are completely symmetrical, that is, $h_1 = h_2 = h$, $l_1 = l_2 = l$, and $k_1 = k_2 = k$, equations (19) can be expressed as

$$\begin{cases} F = 2k(h - d_1) \left(\frac{l}{\sqrt{(h-d_1)^2+a^2}} - 1 \right), \\ (h - d_1) \left(\frac{l}{\sqrt{(h-d_1)^2+a^2}} - 1 \right) = (h - d_2) \left(\frac{l}{\sqrt{(h-d_2)^2+a^2}} - 1 \right), \\ d_1 + d_2 = d. \end{cases} \tag{20}$$

The elastic potential energies in the system are

$$U_1 = 2 \times \tfrac{1}{2} k_1 \Delta l_1^2 = k_1 \left(l_1 - \sqrt{(h - d_1)^2 + a^2} \right)^2,$$
$$U_2 = 2 \times \tfrac{1}{2} k_2 \Delta l_2^2 = k_2 \left(l_2 - \sqrt{(h - d_2)^2 + a^2} \right)^2,$$
$$U = U_1 + U_2 = k_1 \left(l_1 - \sqrt{(h - d_1)^2 + a^2} \right)^2 + k_2 \left(l_2 - \sqrt{(h - d_2)^2 + a^2} \right)^2. \tag{21}$$

We solve equations (20) and (21) by MATLAB and set the spring stiffness $k = 1,000$ N/m.

Appendix B: Stiffness of variable-stiffness structure

The theoretical results, simulation results, and test results of the stiffness of the variable-stiffness structure with different compression are shown in Table B1. We can see that the stiffness measured by the test is within three times of that predicted by the finite element simulation. Except for the fourth stage, the theoretical stiffness, simulation stiffness, and experimental stiffness differ by about three times.

Table B1. *Theoretical results, simulation results, and test results of the variable-stiffness.*

Compression (mm)	Theoretical stiffness (N/m)	Simulation stiffness (N/m)	Test stiffness (N/m)
$d_1 = 1$	1.1195e4	1.168e4	4.082e3
$d_2 = 2$	4.432e4	3.645e4	1.272e4
$d_3 = 3$	2.0276e5	1.303e5	7.165e4
$d_4 = 4$	7.9607e6	1.125e6	1.4086e6

Appendix C: Frequency response curves of the tunable metamaterial

The frequency response curves of the finite periodic structure with different compressions are shown in Figure C1, where the purple bands represent the vibration attenuation zones (where the vibration transmissibility $T < 1$). The location and width of the attenuation zones are shown in Table C1, which are consistent with the bandgap in the infinite periodic structure.
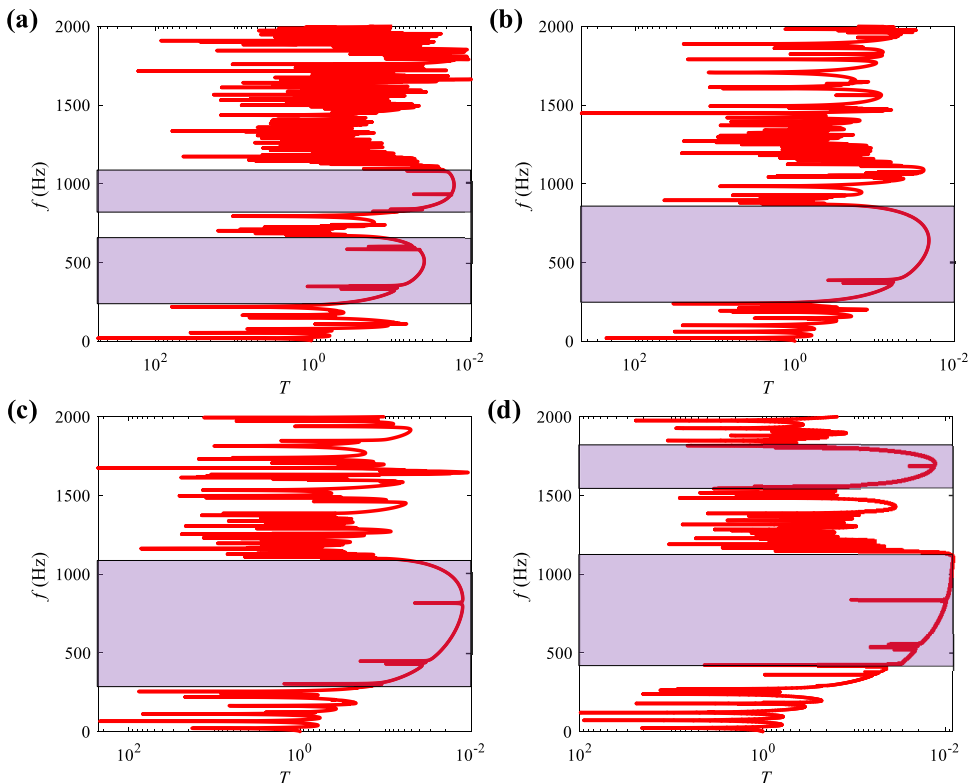

Figure C1. *Frequency response curves of the finite periodic structure: (a) Compression $d_1 = 1$ mm; (b) Compression $d_2 = 2$ mm; (c) Compression $d_3 = 3$ mm; (d) Compression $d_4 = 4$ mm.*

Table C1. *Attenuation zones of tunable metamaterial with different compressions.*

Compression (mm)	Dynamic stiffness (N/m)	Location of the attenuation zone (Hz)	Width of the attenuation zone (Hz)
$d_1 = 1$	5.5781e4	219–685	466
		749–1,138	344
$d_2 = 2$	1.8167e5	239–870	631
$d_3 = 3$	4.3914e5	304–1,109	805
$d_4 = 4$	9.0901e5	424–1,148	724
		1,560–1,801	241